General relativistic magnetohydrodynamic simulations of accretion disks around tilted binary black holes of unequal mass

Milton Ruiz,[1,2] Antonios Tsokaros,[2,3] and Stuart L. Shapiro[2,3,4]

[1]*Departamento de Astronomía y Astrofísica, Universitat de Valéncia, Dr. Moliner 50, 46100, Burjassot (València), Spain*

[2]*Department of Physics, University of Illinois at Urbana-Champaign, Urbana, Illinois 61801, USA*

[3]*National Center for Supercomputing Applications, University of Illinois at Urbana-Champaign, Urbana, Illinois 61801, USA*

[4]*Department of Astronomy, University of Illinois at Urbana-Champaign, Urbana, Illinois 61801, USA*

(Received 17 February 2023; accepted 20 November 2023; published 18 December 2023)

We perform general relativistic simulations of magnetized, accreting disks onto spinning black hole binaries with mass ratio $q \equiv M_{1,\mathrm{irr}}/M_{2,\mathrm{irr}} = 1, 2$ and 4. The magnitude of the individual dimensionless black hole spins are all $\chi = 0.26$ and lie either along the initial orbital plane or 45° above it. We evolve these systems throughout the late inspiral, merger and postmerger phases to identify the impact of the black hole spins and the binary mass ratio on any jet and their electromagnetic (Poynting) signatures. We find that incipient jets are launched from both black holes regardless of the binary mass ratio and along the spin directions as long as the force-free parameter $B^2/(8\pi\rho_0)$ in the funnel and above their poles is larger than one. At large distances the two jets merge into a single one. This effect may prevent the electromagnetic detection of individual jets. As the accretion rate reaches a quasistationary state during the late predecoupling phase, we observe a sudden amplification of the outgoing Poynting luminosity that depends on the binary mass ratio. Following the merger, the sudden change in the direction of the spin of the black hole remnant with respect to the spins of its progenitors causes a reorientation of the jet. The remnant jet drives a single, high-velocity, outward narrow beam collimated by a tightly wound, helical magnetic field which, in turn, boosts the Poynting luminosity. This effect is nearly mass-ratio independent. During this process, a kink is produced in the magnetic field lines, confining the jet. The kink propagates along the jet but rapidly decays, leaving no memory of the spin shift. These results suggest that the merger of misaligned, low-spinning, black hole binary mergers in low-mass disks does not necessarily provide a viable scenario to explain x-shaped radio galaxies if other features are not taken into account. However, the sudden changes in the outgoing luminosity at the merger may help to identify mergers of black holes in active galactic nuclei, shedding light on black hole growth mechanisms and the observed co-evolution of their host galaxies.

DOI: 10.1103/PhysRevD.108.124043

I. INTRODUCTION

Accreting black holes (BHs) are ubiquitous in the Universe. BH masses typically lie between a few solar masses to more than $10^9 M_\odot$ for the most extreme supermassive objects (SMBHs). On the low-mass end, the typical remnant of binary neutron star or black hole-neutron star mergers is a highly spinning BH surrounded by a torus of gas debris (see e.g. [1–3]). On the high-mass end, there is strong observational evidence that most galaxies harbor SMBHs in their centers [4,5], and hence, it is expected that when two galaxies merge, a supermassive black hole binary (SMBHBH) with a separation $\lesssim$100 kpc is formed (see e.g. [6]). Dynamical friction and star ejection bring the binary to pc-scale separation and, simultaneously, the BHs carve out a low-density, inner cavity just outside their orbit, beyond which a circumbinary accretion disk forms [7,8].

As the accretion takes place, electromagnetic (EM) radiation is produced from tenuous hot plasma in the disk and, in most cases, from the magnetically dominated outgoing jet launched from the poles of the BHs and its interactions with the environment (see e.g. [9–11]). This radiation may be detectable by multiple EM instruments, such as FERMI [12], the Event Horizon Telescope [13], PanSTARRS [14], the HST [15], and JWST [16], to name just a few. Gravitational waves (GWs) from inspiralling BHBHs, or even their BH-disk remnants [17,18], have been, or are expected to be, detected either by ground- or space-based GW observatories (see e.g. [19–22] and references therein). Therefore, the possibility of coincident detection of gravitational radiation with EM radiation from these systems makes them prime sources for multimessenger astronomy.

However, multimessenger observations of accreting BHs call for a detailed understanding of the environment

surrounding them, and simultaneously, the identification of the "smoking guns" that can be used to distinguish these systems from other EM sources. Theoretical work on accreting BHs to date has sought to identify characteristic EM features that may accompany GW signals (see e.g. [9,23–34]).

BH-disk systems have been studied in great detail for several decades, progressively incorporating more detailed physical phenomena. Many different disk models ranging from geometrically thin, optically thick to geometrically thick, optically thin disks have been studied (see e.g. [23–26]). All these efforts have been highlighted by the recent, direct imaging of the hot, luminous plasma near the event horizon of the SMBHs at the center of M87 [35] and by Sgr A* in our own Galaxy [36]. In the recently released, high-resolution picture of the Centaurus A (NGC 5128) central core, a SMBH and its accretion disk remain invisible, while its kpc-long relativistic jet has an unexpected shape [37]. It has been suggested that this image may reveal the presence of a SMBHBH with a separation of ∼1 milliparsec instead of a single SMBH [38]. Notice that in all the above theoretical studies, including this one, the gravitational effects from the disk are neglected because typically $M_{\rm disk}/M_{\rm BH} \lesssim 10^{-2}$. Here $M_{\rm disk}$ and $M_{\rm BH}$ are the mass of the disk and BH, respectively. However, some isolated BHs or BHBHs detectable by LISA may find themselves immersed in extended disks with masses comparable or greater than the BHs themselves. This may be particularly true of stellar-mass BHs in active galactic nuclei (AGNs) and quasars due to gravitational drag and *in situ* star formation or SMBHs in extended disks formed in nascent or merging galactic nuclei [39–41]. Recently, we have explored the evolution of self-gravitating disks around tilted, highly spinning BHs with $M_{\rm disk}/M_{\rm BH} \sim 0.2$ [18]. We found that tidal torques from the disk induce a BH spin precession, which can induce a reorientation of the relativistic jet powered by such systems. Such a jet may be observed by various EM instruments.

Studies of accretion onto BHBHs are still immature, and there are still many open questions. In particular, there is no consensus about the environment in the vicinity of the merging BHs. Theoretical efforts involving BHBHs in circumbinary disks that incorporate some degree of relativistic effects and magnetic fields have been launched (see e.g. [9,27–34] and references therein). In [9,31,34] we adopted ideal general relativistic magnetohydrodynamics (GRMHD) to probe EM signatures from magnetized, circumbinary accretion disks onto unequal mass, *nonspinning* BHBHs during the late predecoupling and postdecoupling phases. In all cases, we found that dual magnetically driven jets are launched from the poles of the BHs through the Blandford-Znajek mechanism [42], whose outgoing Poynting luminosity is ∼0.1% of the accretion power. Assuming that there is a mechanism for converting this long-wavelength Poynting flux to small-wavelength emission, this finding may explain x-ray emission in AGNs [43], or γ-ray bursts from stellar-mass BHs, if the disk lifetime is $\sim\mathcal{O}(1)$ s. We also showed that these systems might explain the event GW150914 [44] and its EM counterpart GW150915-GBM reported by the Fermi GBM 0.4 s following the GW observation [45].

The dynamical formation of minidisk structures around spinning BHBHs and their potential EM signatures in full general relativity has been studied recently [46,47] (see also [48,49] for similar studies using an approximate metric for the spacetime evolution). It has been suggested that, as the accretion rate exhibits a quasiperiodic behavior whose amplitude depends on the minidisks, they may be used to estimate BH spins through EM observations in the near future [46,47].

In this work, we extend our own previous studies to consider circumbinary disks around BHBHs with misaligned spins and mass ratios $q \equiv M_{1,\rm irr}/M_{2,\rm irr} = 1, 2$ and 4, starting near the end of the binary-disk predecoupling epoch. Here $M_{\rm i,irr}$, with $i = 1, 2$, is the irreducible mass of the ith BH. The fluid is modeled using a Γ-law equation of state (EOS), $P = (\Gamma - 1)\epsilon\rho_0$. We set $\Gamma = 4/3$, appropriate for radiation pressure-dominated, optically thick disks. The disk is initially threaded by a pure poloidal magnetic field confined to its interior. The magnitude of the individual dimensionless BH spin in all cases is $\chi \equiv S/M_{\rm i,irr}^2 = 0.26$, consistent with a stochastic accretion in AGNs (see e.g. [50,51]), lying either in the initial orbital plane or 45° above it. Here S is the magnitude of the spin angular momentum. We evolve these systems throughout the late inspiral, merger and postmerger phases to identify their unique EM emission features and to analyze the impact of the BHs' spin and the binary mass ratio. In particular, we probe whether the precession or spin shift of the BH remnant with respect to the spins of its progenitors leaves an observable imprint in the outgoing Poynting luminosity, in the profile of the surrounding medium, or in the magnetically driven jet. Such an imprint may be used to characterize the spin of the merging BHBH or give new insights on the formation channels of x-shaped radio galaxies [52,53] as well as on searches for such systems (see e.g. [54]).

Once the accretion rate reaches a quasisteady state during predecoupling, we find that a magnetically driven (dual) outflow inside a helical magnetic funnel emerges from both BHs along the direction of each individual BH spin, as long as the force-free parameter within the funnel $b^2/(2\rho_0) \equiv B^2/(8\pi\rho_0) \gtrsim 1$. Here B is the magnitude of the magnetic field as measured by a comoving observer and ρ_0 is the rest-mass density. However, at large distance from the BHs, where $b^2/(2\rho_0) \lesssim 1$, both funnels merge, pointing in the direction of the total angular momentum of the system. These results are consistent with those recently reported in [11], where misaligned spinning BHBHs, with spin parameter $\chi = 0.6$ and spin lying 45° below the initial

orbital plane, were considered immersed in a cloud of magnetized matter. These studies indicate that EM signatures from individual jets may not be detectable as suggested previously (see e.g. [55]).

During the predecoupling phase, the accretion rate exhibits a quasiperiodic behavior with a dominant frequency $2\pi f_c \simeq (3/4)\Omega_{\rm BHBH}$ regardless of the mass ratio. Here $\Omega_{\rm BHBH}$ is the average orbital frequency of the system. Following the first $\sim 0.14 - 0.36(M/10^6 M_\odot)(1+z)$ h [or $\sim 5 - 14(M/10 M_\odot)(1+z)$ ms], we observe that, depending on the mass ratio, the outgoing Poynting luminosity is significantly boosted. Consistent with [31], we also observe a new, though rather moderate boost in the luminosity during the rebrightening/afterglow phase that is nearly mass-ratio independent. These sudden changes from the jet and from the disk can alter the EM emission and may be used to distinguish BHBH in AGNs from single accreting BHs based on jet morphology [31,56].

During and after the merger, we track the magnetic field lines emanating from the BH apparent horizons and observe a slight kink perturbation propagating along the funnel. This kink can be attributed to the spin shift of the BH remnant with respect to the spin of its progenitors. However, this perturbation is quickly damped in $\Delta t \sim$ few M, leaving no memory of the reorientation of the spin. It has been suggested that the spin of SMBHs is low if accretion is stochastic, which naturally reduces their spin (see e.g. [50,51,57–59]. Therefore, our preliminary results, along with those in [11], suggest that a spin reorientation may not be a plausible scenario to explain x-shaped radio galaxies, although the situation with massive, self-gravitating disks and/or higher spins may be different. Further simulations that will explore a larger parameter space are needed for a definite answer.

It is worth mentioning that the spins of SMBHs inferred from the x-ray observations of AGNs with relativistically broadened Fe Kα lines imply that the spin magnitude of most SMBHs should be $\chi \gtrsim 0.9$ (see e.g. [60–63]), and hence, spin reorientations from highly spinning BHBHs may be a plausible scenario. In fact, for steady accretion from a magnetized disk, the spin will relax to $\chi \gtrsim 0.9$ [64]. As pointed out in [65], GW observations from merging SMBHBHs are required to impose tight constraints on their spin. It has been suggested that the individual BH spins can be reoriented along the total angular momentum of the disk by angular momentum exchange with the accreting matter due to the Bardeen-Petterson mechanism [66]. However, this effect has only been observed in GRMHD simulations of very thin disks with scale heights below $H/R < 0.05$ (see e.g. [67]). There has been no indication that Bardeen-Petterson alignment for thicker accretion disks is possible.

The paper is structured as follows: In Sec. II, we provide a qualitative overview of the evolution of BHBHs in circumbinary disks to motivate the choice of our binary configurations. We also summarize our numerical methods employed for generating initial data and provide a review of the methods used in our numerical evolutions. For further details, readers are referred to [9,31,34]. In Sec. III, we describe our findings and discuss their astrophysical implications. We summarize our conclusions in Sec. V. Geometrized units, where $G = 1 = c$, are adopted throughout unless stated otherwise.

II. METHODS

The dynamics of a BHBH in a circumbinary disk can qualitatively be understood decomposing the evolution in three phases:

(i) The early inspiral predecoupling phase during which the evolution of the system is governed by a binary-disk angular momentum exchange mediated by tidal torques and an effective viscosity. The matter follows the BHBH as it slowly inspirals. Note that Newtonian 2D-viscous and 3D studies, as well as other studies of thin disks incorporating some approximations of relativistic gravity, found that the binary tidal torques carve out a partial hollow at roughly twice the binary separation of the binary (see e.g. [7,8,28,68–76]). However, full GR numerical simulations found that matter can refill the hollow or even (partially) overflow it, hence questioning the above results (see e.g. [9,29,34]);

(ii) The very late inspiral postdecoupling phase, where the orbital separation shrinks due to GW radiation emission. The binary then moves inward faster than the ambient matter, leaving the disk behind with a subsequent decrease in the accretion rate. In contrast to semianalytic calculations claiming that binary torques during this phase quench the accretion (see e.g. [7,77,78]), numerical studies found that the accretion is not completely suppressed [9,29,30,34,68,72,79]. Instead, accretion streams with densities comparable with those in the disk are frequently accreted.

(iii) Finally, the binary merger rebrightening/afterglow phase, where subsequently the matter begins to flow into the "partial" hollow formed during the inspiral. This could lead to bright EM signals, such as: (i) Poynting luminosities associated with magnetically driven jets [31,32,34,80]; (ii) thermal radiation that may give rise a soft x-ray counterpart (to a LISA event lasting a few months after the GW signal [81,82]); and (iii) detectable spectral and light curves [83,84].

As discussed above, the disk structure at decoupling has a key role in determining the subsequent evolution and the EM emission. The inner part of the disk settles into a quasiequilibrium state on the viscous timescale,

$$t_{\rm vis} \sim \frac{2}{3}\frac{R_{\rm in}^2}{\nu}, \tag{1}$$

where ν is the effective viscosity induced by MHD turbulence [85], and $R_{\rm in}$ is the radius of the disk inner edge. This viscosity can be approximately fit to an α-disk law for an analytic estimate, i.e.

$$\nu(R) = \frac{2}{3}\alpha(P/\rho_0)\Omega_{\rm K}^{-1} \approx \frac{2}{3}\alpha(R/M)^{1/2}(H/R)^2 M, \quad (2)$$

where H is the half-thickness of the disk and M the total mass of the BHBH. Notice that in the above expression, we have assumed vertical hydrostatic equilibrium to derive an approximate relationship between P/ρ_0 and H/R [86]. In the early stage of the BHBH evolution, the GW inspiral timescale $t_{\rm GW}$ can be estimated as [87]

$$t_{\rm GW} \approx \frac{5}{16}\frac{a^4}{M^3\eta}, \quad (3)$$

where a is the binary separation, and $\eta \equiv 4q/(1+q)^2$ is the reduced mass, with mass ratio $q \equiv M_{1,\rm irr}/M_{2,\rm irr} > 1$. Equating the viscous timescale and the GW inspiral timescale, and assuming that $R_{\rm in} = \beta a$, yields the decoupling separation [9,34]

$$\frac{a_d}{M} \approx 11.5\left(\frac{\beta}{1.3}\right)^{3/5}\left(\frac{\eta}{1}\right)^{2/5}\left(\frac{\alpha}{0.1}\right)^{-2/5}\left(\frac{H/R}{0.3}\right)^{-4/5}, \quad (4)$$

where the normalizations are based on the values found in our simulations described below. This estimate suggests that the initial orbital separation of BBH models in the predecoupling phase should be set to be larger than $\sim 11.5M$. In what follows, we consider spinning binaries on a quasicircular orbit with mass ratio $q = 1, 2$, and 4. Table I summarizes the initial parameters of these systems. Consistent with the above estimate, we observe that the binaries undergo ~ 11 quasicircular obits before entering the postdecoupling phase (see below). This allows the disk (at least the inner part) to relax, giving rise to a quasistationary accretion flow.

TABLE I. Two puncture initial data parameters for quasicircular, spinning BHBH spacetimes. Columns display the case name, the mass ratio ($q \equiv M_{1,\rm irr}/M_{2,\rm irr} \geq 1$), defined as the ratio of the BH irreducible masses, the direction and magnitude of the dimensionless BH spin, the binary coordinate separation (a/M), the binary angular velocity ΩM, and total ADM angular momentum J/M^2. Here M is the ADM mass of the system. In all cases, we set $S_x = 0$, and hence, the magnitude of the individual dimensionless BH spin is $\chi = S/M_{\rm irr}^2 = 0.26$.

Case	q	$S_y/M_{\rm i,irr}^2$	$S_z/M_{\rm i,irr}^2$	a/M	ΩM	J/M^2
q1	1	0.26	0.0	14.0	1.74×10^{-2}	1.07
q2	2	0.184	0.184	13.25	1.89×10^{-2}	1.03
q4	4	0.184	0.184	12.5	2.04×10^{-2}	0.78

A. Metric initial data

Following [34], we use the TwoPunctures code [88] to build the spacetime metric. We set the binaries on a quasicircular orbit at a coordinate orbital separation $\gtrsim 12.5M$ (see Table I). Here M is the ADM mass of the binary, which is arbitrary. To probe the effects of the mass ratio and the direction of the BHs' spin on the EM signatures and jet, we consider unequal mass BHBHs ($q = 1, 2$ and 4) and set the magnitude of the individual dimensionless BH spin to $\chi = 0.26$, lying either in the initial orbital plane ($q = 1$ case) or 45° above it ($q = 2$ and $q = 4$ cases; see inset in Fig. 1), as in [89]. We consider BHs with a "low-spin" parameter to match those assuming that the accretion onto the BHs is stochastic (see. e.g. [50,51,57–59]). It even has been argued that SMBH growth in an AGN occurs via sequences of randomly oriented accretion disks, and hence, the BH spin parameter could be smaller ranging between $\chi \sim 0.1$ and ~ 0.3 [50]. As we describe below, our configurations undergo $\gtrsim 14$ orbits before the merger, allowing the individual BH spins to precess between half and a full cycle before the merger (see Fig. 2). Details of the initial BHBH configurations are summarized in Table I.

B. Fluid and magnetic field initial data

For the fluid, we use the equilibrium solutions of a stationary disk around a single Kerr BH as in e.g. [90,91] with the same mass as the ADM mass of the BHBH and adopting a Γ-law EOS, $P = (\Gamma - 1)\epsilon\rho_0$. In all models in Table I, we set $\Gamma = 4/3$, which is appropriate for radiation pressure-dominated, optically thick disks (see e.g. [92]). The disk equator lies in the orbital x-y plane of the binary. Following [9,34], we choose the initial inner disk edge radius $R_{\rm in} = 18M$ and the specific angular momentum $l(R_{\rm in}) = 5.25M$. The resulting disk has a peak pressure at $\sim 30M$. Notice that in our configurations, we had to choose different coordinate binary separations a/M while keeping the same accretion disk. This allowed us to evolve these systems from the inspiral all the way to the postmerger phase with the computational resources we had at our disposal.

It is worth mentioning that our numerical studies of the BHBH-disk in [9] found that by keeping the orbital separation fixed at $10M$, the accretion rate for a disk with the above initial inner radius settles to a steady value after a few thousand M, an indication that the inner disk edge has relaxed. In our cases, here, it is expected that the accretion will settle earlier, since the BHs are closer to the disk, allowing the gravitational torques to plunder the inner layers of the disk easier than those above [34].

As in [9,34], the accretion disk is initially threaded with a dynamically unimportant, purely poloidal magnetic field

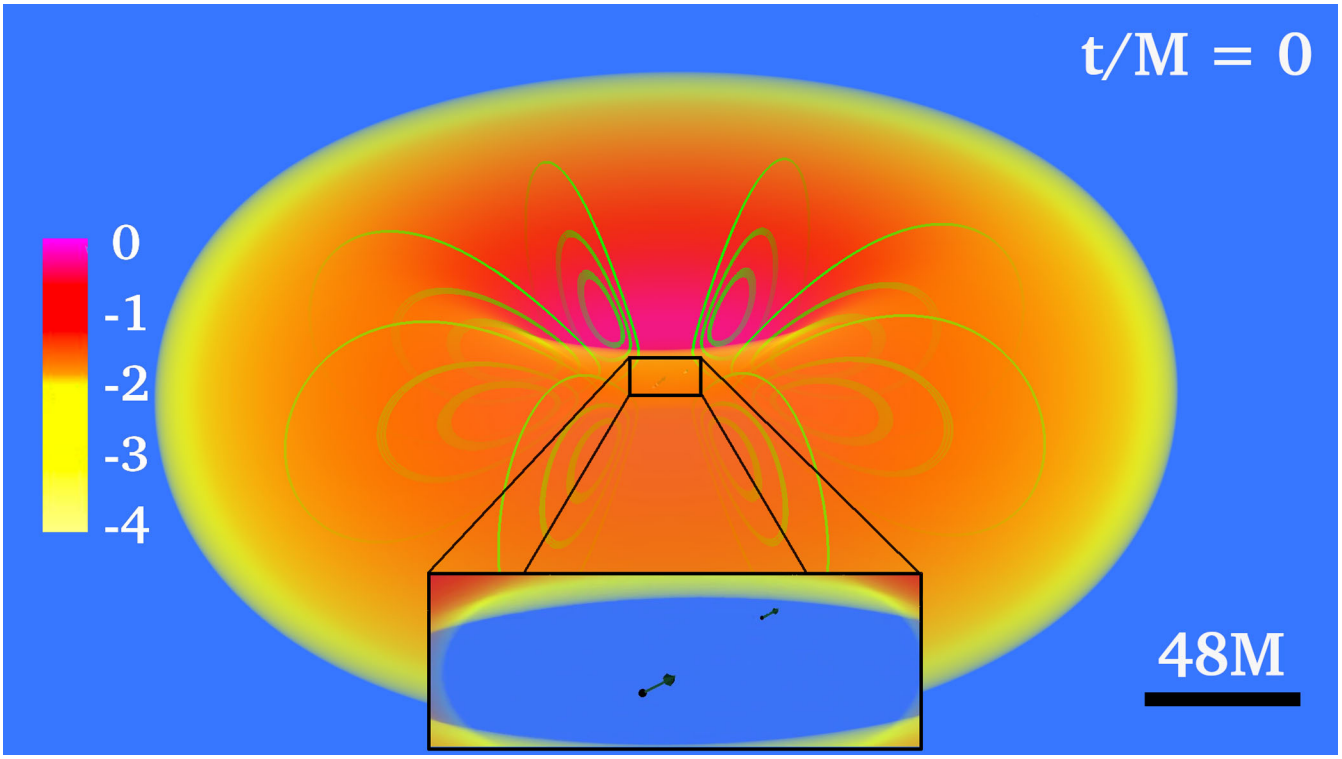

FIG. 1. Volume rendering of the rest-mass density normalized to its maximum value at $t = 0$ for a BHBH with mass ratio $q = 2$ (see Table I). The disk is threaded by a pure poloidal magnetic field (green lines) confined to its interior. The inset highlights the coordinate position of the BH apparent horizons (black spheres) and the direction of the individual BH spins (dark green arrow).

that is confined to its interior (see Fig. 1). This field is generated by the vector potential

$$A_i = \left(-\frac{y}{\varpi^2}\delta^x{}_i + \frac{x}{\varpi^2}\delta^y{}_i\right)A_\varphi, \tag{5}$$

$$A_\varphi = A_B \varpi^2 \max(P - P_{\rm cut}, 0), \tag{6}$$

where $\varpi^2 = x^2 + y^2$, A_B, and $P_{\rm cut}$ are free parameters. The cutoff pressure parameter $P_{\rm cut}$ confines the magnetic field inside the disk to lie within the region where $P_{\rm gas} > P_{\rm cut}$. We choose $P_{\rm cut}$ to be 1% of the maximum pressure. The parameter A_B determines the strength of the magnetic field and can be characterized by the magnetic-to-gas-pressure ratio, which we set to $P_{\rm mag}/P_{\rm gas} \approx 0.01$.

Our disk models are unstable to the magnetorotational instability (MRI), which induces an effective turbulent viscosity allowing angular momentum transport and accretion to take place. As pointed out in [9,34] in our disk: (i) we choose a rotation profile satisfying $\partial_r \Omega < 0$, with

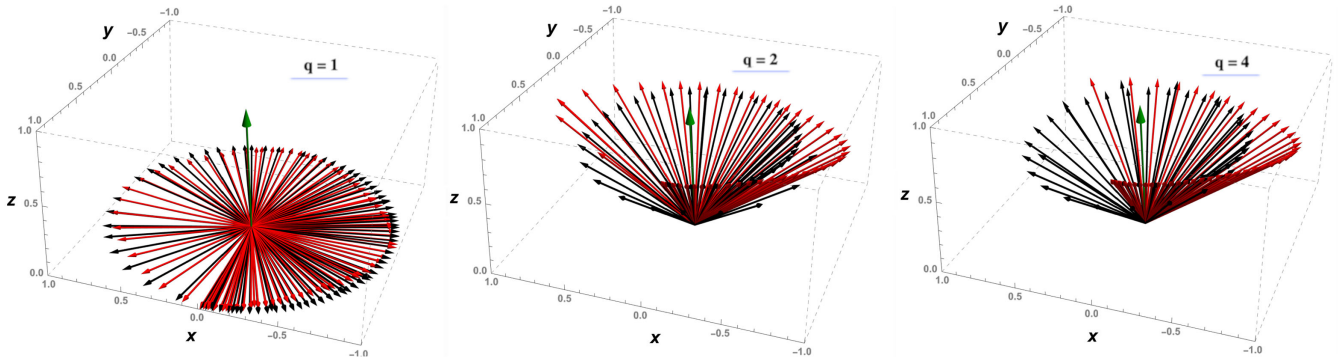

FIG. 2. Spin direction of each individual apparent horizon during inspiral (red arrows display the spin direction of the primary BH, while those in black display the spin direction of the secondary) and the spin direction of the BH remnant following the merger (green arrow) for all cases in Table I. The arrows are plotted every $\Delta t \sim 40M$. Notice that the arrows indicate only the spin direction but not its magnitude.

$\Omega = u^{\phi}/u^{t}$ the fluid angular velocity [93]; (ii) in the bulk of the disk, we resolve the wavelength of the fastest growing MRI mode $\lambda_{\rm MRI}$ by $\gtrsim$20 gridpoints [9], except for the region near a radius where the magnetic field flips sign and becomes very small (see top panel in Fig. 3); and (iii) the strength of the magnetic field is low enough for $\lambda_{\rm MRI}$ to fit inside the disk (see bottom panel in Fig. 3). Figure 4 displays the λ-MRI-quality factor at selected times along with the rest-mass density for $q = 1$ showing that during the evolution our numerical resolution is sufficient to resolve this instability. Similar behavior is found in all our cases.

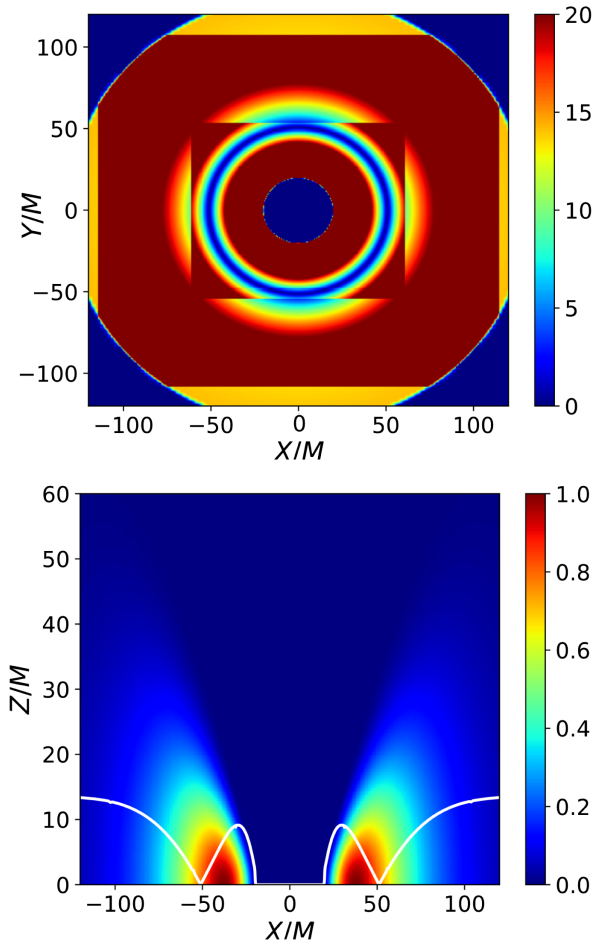

FIG. 3. Top panel: contours of the $\lambda_{\rm MRI}$-quality factor $Q = \lambda_{\rm MRI}/dx$ on the equatorial plane for case $q = 1$. Notice that with the numerical resolution employed in our simulations, the fastest growing MRI mode is resolved by $\gtrsim$20 gridpoints over a large part of the disk except in a small region (blue ring) when the vertical component of the magnetic field changes sign. Bottom panel: initial rest-mass density contours (color coded) normalized to its maximum value on a meridional slice along with the $\lambda_{\rm MRI}/2$ (white solid line) demonstrating that the latter fits in the bulk of the disk. Similar results are found among all cases considered in Table I.

C. Numerical setup

1. Evolution method

We use the extensively tested Illinois GRMHD code [94], which is embedded in the Cactus infrastructure [95] and employs the Carpet code [96,97] for moving-box mesh capability. For the metric evolution, this code solves the Baumgarte–Shapiro–Shibata–Nakamura (BSSN) equations [98,99], coupled to the puncture gauge conditions cast in first order form [see Eqs. (14)–(16) in [100]]. The code adopts fourth-order, centered, spatial differencing, except on shift advection terms, where fourth-order upwind differencing is used. For the damping coefficient η_β appearing in the shift condition, we use a spatially varying coefficient, as was done in the numerical simulations of the Numerical-Relativity-Analytical-Relativity (NRAR) collaboration (see Table III in [101]). For the matter and magnetic field, the code solves the equations of ideal GRMHD in flux-conservative form [see Eqs. (21)–(24) in [100]] employing a high-resolution-shock-capturing scheme. To enforce the zero-divergence constraint of the magnetic field, we solve the magnetic induction equation using a vector potential formulation. To prevent spurious magnetic fields arising across refinement levels, we adopt the generalized Lorenz gauge [102].

To verify the reliability of the BHBH evolution, we implement a number of several local and global diagnostics as in [9]. For example, we monitor the value of the L_2 norm of the normalized Hamiltonian and momentum constraint violations as introduced in Eqs. (40) and (41) in [100], where the Laplacian operator is separated in its individual components when computing normalized norms. During the whole evolution, the constraints remain $\lesssim$1%, peak at $\lesssim$2% during the merger and finally settle back to $\lesssim$1% after the BH-disk remnant reaches quasiequilibrium.

2. Grid structure

We use a set of three nested refinement boxes, with one centered on each BH and one set centeterd on the binary center of mass. In all cases, we use 10 boxes centered on the primary BH, while for the secondary one, we use between 10 to 12 boxes depending on the mass ratio (i.e. depending on the initial size of the secondary BH's apparent horizon). The coarsest level has an outer boundary at $384M$ (see Table II). This hierarchical mesh structure allows us to resolve each individual apparent horizon by at least $\sim$26 grid points across its radius and, simultaneously, to have enough resolution in the bulk of the disk to resolve $\lambda_{\rm MRI}$ by $\gtrsim$20 gridpoints (see Fig. 3).

III. RESULTS

Our simulations are primarily designed to identify EM features associated with the jets that can be, along with gravitational radiation, used to observationally infer some

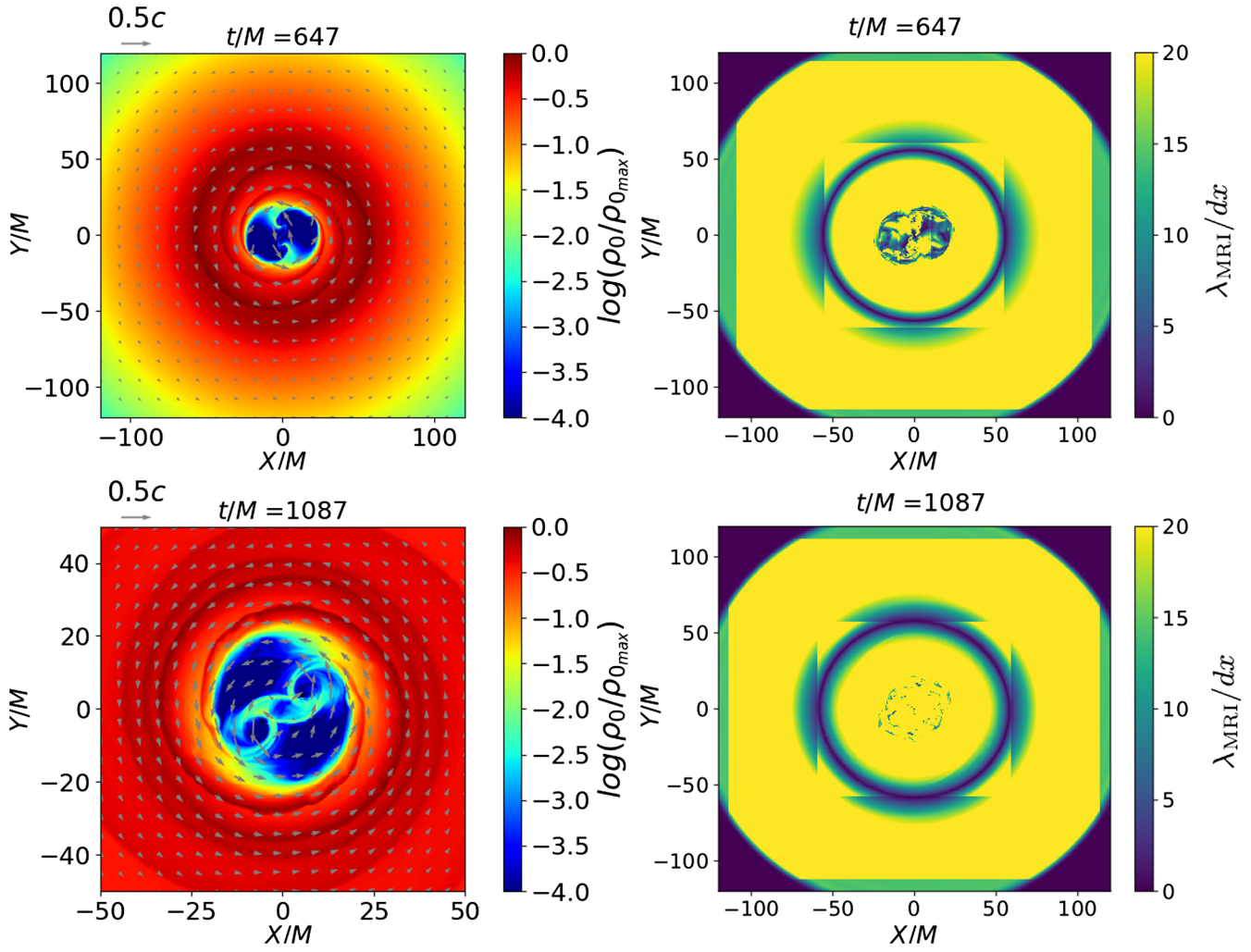

FIG. 4. Rest-mass density normalized to its initial maximum value (left column) and contours of the $\lambda_{\rm MRI}$-quality factor (right column) on the equatorial plane at selected times for case $q = 1$. With the numerical resolution employed in our simulations, the fastest growing MRI mode is resolved by $\gtrsim$20 gridpoints over a large part of the disk during the evolution. Similar results are found among all cases considered in Table I.

physical properties of BHBH, such as mass ratios, BH spin, etc. A GR calculation is necessary to accurately determine the accretion rate onto the BHs and to determine the flow and emission from the strong-field regions near the BHs. The motivation for our study is to address the following question:

Is the reorientation of the spin direction of the BH remnant and associated jet, with respect to the spins of its progenitors, a viable mechanism to explain x-shaped radio galaxies?

As discussed previously, we consider "low-spin" binaries consistent with a stochastic accretion that naturally

TABLE II. List of grid parameters for all models listed in Table I. The computational mesh consists of three sets of nested moving grids, one centered on each BH and one on the binary center of mass, with the outer boundary at $380M$ in all cases. Here the columns indicate case label, the coarsest grid spacing $\Delta x_{\rm min}$, the number of refinement levels around each BHs and their half length. The grid spacing of all other levels is $\Delta x_{\rm max}/2^{n-1}$, with $n = 1, \ldots, n_{\rm max}$, where $n_{\rm max}$ is the level number.

Case	$\Delta x_{\rm min}$	Levels $\rm BH_1$	Levels $\rm BH_2$	Grid hierarchy (in units of M)
q1	$3.84M$	10	10	$384M/2^{n-1}$, $n = 1, \ldots, 5$; $512M/2^n$, $n = 6, \ldots, 10$
q2	$3.84M$	11	10	$384M/2^{n-1}$, $n = 1, \ldots, 5$; $512M/2^n$, $n = 6, \ldots, 11$
q4	$3.84M$	12	10	$384M/2^{n-1}$, $n = 1, \ldots, 5$; $512M/2^n$, $n = 6, \ldots, 12$

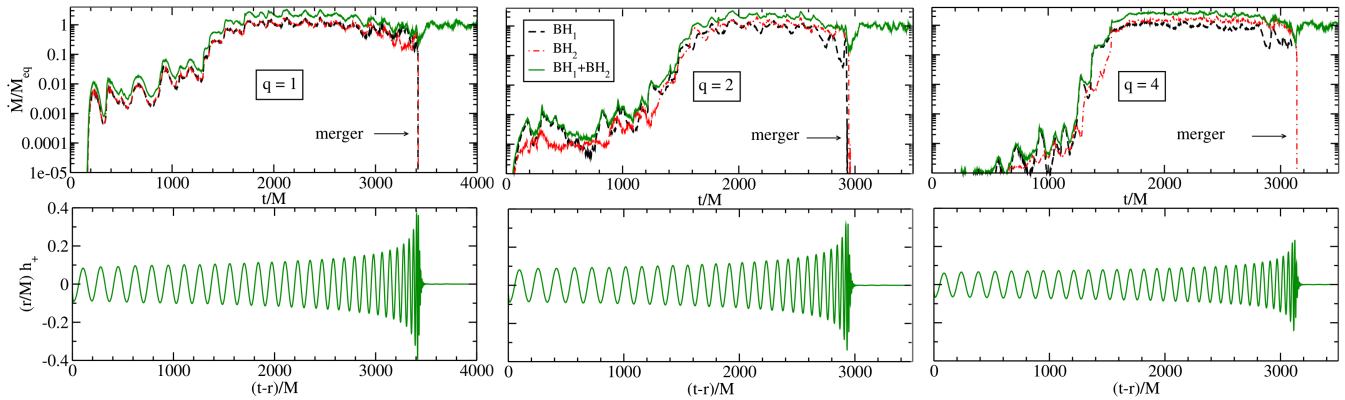

FIG. 5. Top panel: accretion rate $\dot{M}$ onto the primary BH (red, dashed line), onto its companion (black, solid line), and their sum (green, solid line) for all cases listed in Table I. The normalization $\dot{M}_{\rm eq}$ is the time-averaged accretion rate onto the BH remnant over the last $\Delta t \sim 500M$ before the termination of our simulations. Bottom Panel: GW strain h_+^{22} (dominant mode) vs retarded time.

reduces the BH spin. We will explore high spinning BHBHs, consistent with x-ray observations of AGNs with relativistically broadened Fe Kα lines, in future investigations. We also consider low-mass disks here with negligible self-gravity. We will treat high-mass disks with significant self-gravity in future studies as well.

A. Accretion rates

In contrast to the nonspinning BHBH in our previous accretion disk studies [9,34], where the accretion takes place in the orbital plane, we observe that during the initial phase of the binary inspiral, tidal torques strip matter from the inner disk's edge, which induces the formation of spiral arms that continuously feed the BHs on a plane perpendicular to the direction of each individual spin. Similar behavior has been reported on the misaligned spinning BHBHs immersed in a magnetized cloud of matter recently reported in [11] and in the misaligned, highly (extremal) spinning BHs surrounded by self-gravitating disks [18].

The top panel in Fig. 5 displays the accretion rates $\dot{M}$ through the BH's apparent horizons during the whole evolution, as introduced in Eq. (A11) in [92]. During roughly the first ∼5 quasicircular orbits (or $\Delta t \sim 1500M$; see bottom panel in Fig. 5), we observe that when the mass ratio $q > 1$, matter is more efficiently swallowed by the primary BH than by the secondary, where a low-density, disklike structure tends to pile up around it periodically. This result is consistent with the studies in [31,46,48] showing that if the Hill sphere is well outside of the innermost stable circular orbit (ISCO), a persistent disklike structure (the so-called minidisks) can form around a BH. In our cases (see Table I), the Hill sphere for the secondary BH can be estimated as $r_{\rm Hill} \equiv a(3q)^{-1/3}/2 \sim 4M(a/11.5M)q^{-1/3}$. Thus, for $q = 4$, we find that $r_{\rm Hill} \sim 2.8M > r_{\rm ISCO} \sim 1M$. Similarly, for $q = 2$, we find that $r_{\rm Hill} \sim 2r_{\rm ISCO} \sim 3.5M$, and $r_{\rm Hill} \sim 2r_{\rm ISCO} \sim 5M$ for $q = 1$. These estimates explain why we observe quasiperiodic modulations in the accretion rate (see top Panel in Fig. 5) in $q = 1$ and in the secondary BH for the other two cases: There is enough room between $r_{\rm Hill}$ and for $r_{\rm ISCO}$ matter to wrap around the BHs, forming transient minidisks, which, in turn, reduce the accretion. Note that persistent minidisks that form when $r_{\rm Hill} \gg r_{\rm ISCO}$ can significantly reduce the accretion [46,47] with respect to those cases when $r_{\rm Hill} \sim r_{\rm ISCO}$. Thus, during the early inspiral, the quasiperiodic behavior in $\dot{M}$ is dominated by the secondary BH.

Following the early inspiral, we observe that, in all cases, $\dot{M}$ gradually reaches a quasiequilibrium state. Notice that our BHBH-disk configuration reaches a quasiequilibrium state at different times. In particular, cases $q = 1$ and $q = 4$ reach quasiequilibrium by $t \sim 1500M$ and $t \sim 1400M$, respectively. After this point, the system remains nearly stationary for the next ∼5–6 orbits (∼$1000M$). Figure 9 displays rest-mass density contour at selected times during the predecoupling phase on the xz plane. During this lapse of time, which is over a rotation period in the inner disk, the density does not change significantly, a further indication that the disk has achieved a steady state.

During this period, we compute the averaged accretion rate for cases $q = 2$ and $q = 4$ and find that in the former, the averaged accretion rate onto the primary BH is ∼16% larger than the rate on its companion. However, for the latter case, the accretion onto the primary BH is 38% larger. This difference is expected, since the effective cross section of the secondary BH, which depends on its irreducible mass, is smaller. We note that these results are consistent with the 2D hydrodynamical Newtonian simulations of thin disks around nonspinning BHBH with a mass-ratio ranging between 1 and ∼38 reported in [30] the dominant contribution to the total accretion rate comes from the primary BH, as well as with those from GRMHD of nonspinning BHBHs with $q \leq 10$ reported in [9]. Notice that the accretion rate may be also affected by the direction of the individual BH spins. The simulations of BHBHs with

TABLE III. Summary of main results. Columns display case name, merger time defined as the time of GWs peak amplitude. Followed by the mass, the spin and the kick velocity of the BH remnant in $\mathrm{km\,s^{-1}}$. Next, the time-averaged accretion rate onto the BH remnant over the last $\Delta t \sim 500M$ before the termination of our simulations, the Poynting radiative efficiency $\epsilon_{\rm EM} = L_{\rm EM}/\dot{M}$ and the Lorentz factor in the funnel after the outflow has reached quasiequilibrium following merger. Notice that the accretion mass in each evolved case is normalized to the $\dot{M}$ of its corresponding BH remnant over the last $\Delta t \sim 500M$. We use A1 in [34] to recover the corresponding physical units.

Case	$t_{\rm mer}$	$M_{\rm BH}$	$S_z/M_{\rm irr}^2$	$v_{\rm kick}$	$\dot{M}/\dot{M}_{\rm eq}$ [a]	$\epsilon_{\rm EM}$	W
q1	3425	$0.94M$	0.78	3	1.23	0.030	2.6
q2	2962	$0.96M$	0.74	230	1.30	0.026	2.1
q4	3148	$0.98M$	0.60	170	1.38	0.024	1.6

[a] $\dot{M}_{\rm eq} \sim 10^{-2}\left(\frac{\rho_0}{10^{-11}\ \mathrm{gm/cm^3}}\right)\left(\frac{M_{\rm BH}}{10^6 M_\odot}\right)^2 M_\odot\ \mathrm{yr}^{-1}$.

spin $\chi = \pm 0.9$ reported in [74], where an approximate metric for the spacetime evolution is used, found that the accretion is enhanced by 45% (or reduced by ∼14%) for the anitaligned (aligned) case with respect to the nonspinning cases.

To probe periodicity features in the accretion rate that may give rise to periodic EM signatures, we perform a Fourier analysis as in [9,34]. We find that, regardless the mass ratio, the total accretion rate $\dot{M}_{\rm BHBH}$ (i.e. the accretion mass onto both BHs) exhibits a dominant frequency $2\pi f_{\rm c} \simeq (3/4)\Omega_{\rm BHBH}$. Here $\Omega_{\rm BHBH}$ is the average orbital frequency determined during the predecoupling phase from the GWs. This characteristic frequency is roughly the same as that found in our GRMHD studies of circumbinary disks around nonspinning BHBHs with mass ratio $q = 36/29$ in [34], though slightly smaller than $2\pi f_{\rm c} \simeq (4/3)\Omega_{\rm BHBH}$ found in our GRMHD studies of equal-mass, nonspinning BHBHs in [9,29] where it has been attributed to the Lindblad resonance [68]. Similar results have been reported in [28,33,76] using an approximate metric for the spacetime evolution. In addition, the GRMHD studies in [9], where an effective radiative cooling process was also considered, found a single peak frequency at $\Omega_{\rm BHBH}$ in $q = 4$. Our results suggest that periodicity signatures in the accretion rate during the predecoupling phase are not sensitive to the binary mass ratio, to the BH spin, or to the geometric thickness of the disk. The latter is suggested in [34]. These results may be used potentially to infer the binary frequency from EM observations when the GWs are too weak, though realistic cooling processes are required to reliably determine how the variability in the accretion rate maps onto EM signatures. These results are roughly consistent with the Newtonian simulations in [30,68,103] of a merging BHBH in a geometrically thin disk with mass ratio $q < 10$ and an α-viscosity prescription that found that $2\pi f_{\rm c} \simeq \Omega_{\rm BHBH}$. This frequency has been attributed to the BHs passing near the inner edge of the disk striping material. However, these simulations found that for mass ratio $q \gtrsim 10$, the characteristic frequency of the accretion rate strongly depends on the mass ratio. The binary induces eccentricity in the inner region of the disk, driving the formation of overdense lumps, which enhance periodicity patterns in the accretion rate. This effect may provide a method for observationally inferring mass ratios from luminosity measurements that give the inferred accretion rate. However, GRMHD simulations of BHBH in geometrically thick disks found a rather complex structure in the Fourier spectrum of $\dot{M}$ [9]. These differences have been attributed mainly to the different turbulent viscosity prescriptions.

Once the system reaches the postdecoupling phase (roughly after 11 quasicircular orbits; see bottom panel in Fig. 5), the accretion rate gradually decreases as the BHBH inspiral speeds up until the merger. Following the merger, low-density material refills the partial hollow left by the binary causing the accretion to ramp up once again. As the spinning BH remnant reaches a quasisteady state, the accretion for $q = 1$ settles to ∼40% of the maximum value of the rate reached during the binary inspiral, while it settles at ∼43% and ∼48% of the maximum value of the accretion rate for $q = 2$ and $q = 4$, respectively. The trend is that the smaller the spin of the BH remnant (the larger the ISCO; see Table III), or equivalently, the larger the binary mass ratio of the progenitors, the larger the relative accretion rate.

Anisotropic emission of GWs and momentum conservation produces a recoil or "kick" of the BH remnant, which can have a significant impact on the accretion flow. However, in our $q = 2$ and $q = 4$ cases, the kick velocity is $\lesssim 230$ km/s (see Table III), and hence, it is small compared to other characteristic velocities in the system [104]. It is expected that these kicks do not have any significant impact on the accretion.

IV. OUTFLOWS AND JETS

Figure 6 displays our 3D visualizations of the rest-mass density along with magnetic field lines during the late predecoupling (left column) and rebrightening/afterglow (right column) phases. During the former (i.e. once the accretion reaches a quasistationary state), the magnetic pressure above the poles of each individual BH increases as net poloidal magnetic fluxes are accreted onto them. This in turn leads to the formation of a helical funnel bounded by the magnetic field lines emanating from the BHs. These funnels lie along the direction of the BHs' spin and form as long as the force-free parameter is $b^2/(2\rho_0) \gtrsim 1$ (i.e. along magnetically dominated regions). However, at larger distances from BH poles, where the magnetic-to-gas-pressure ratio decays to values $\lesssim 1$, the funnels are reoriented in the direction of the total angular momentum of the system. In particular, the primary BH's funnel in $q = 4$ extends a distance of $r \sim 10 r_{\rm BH}$ along the direction of its spin and then is reoriented along the total angular momentum of the

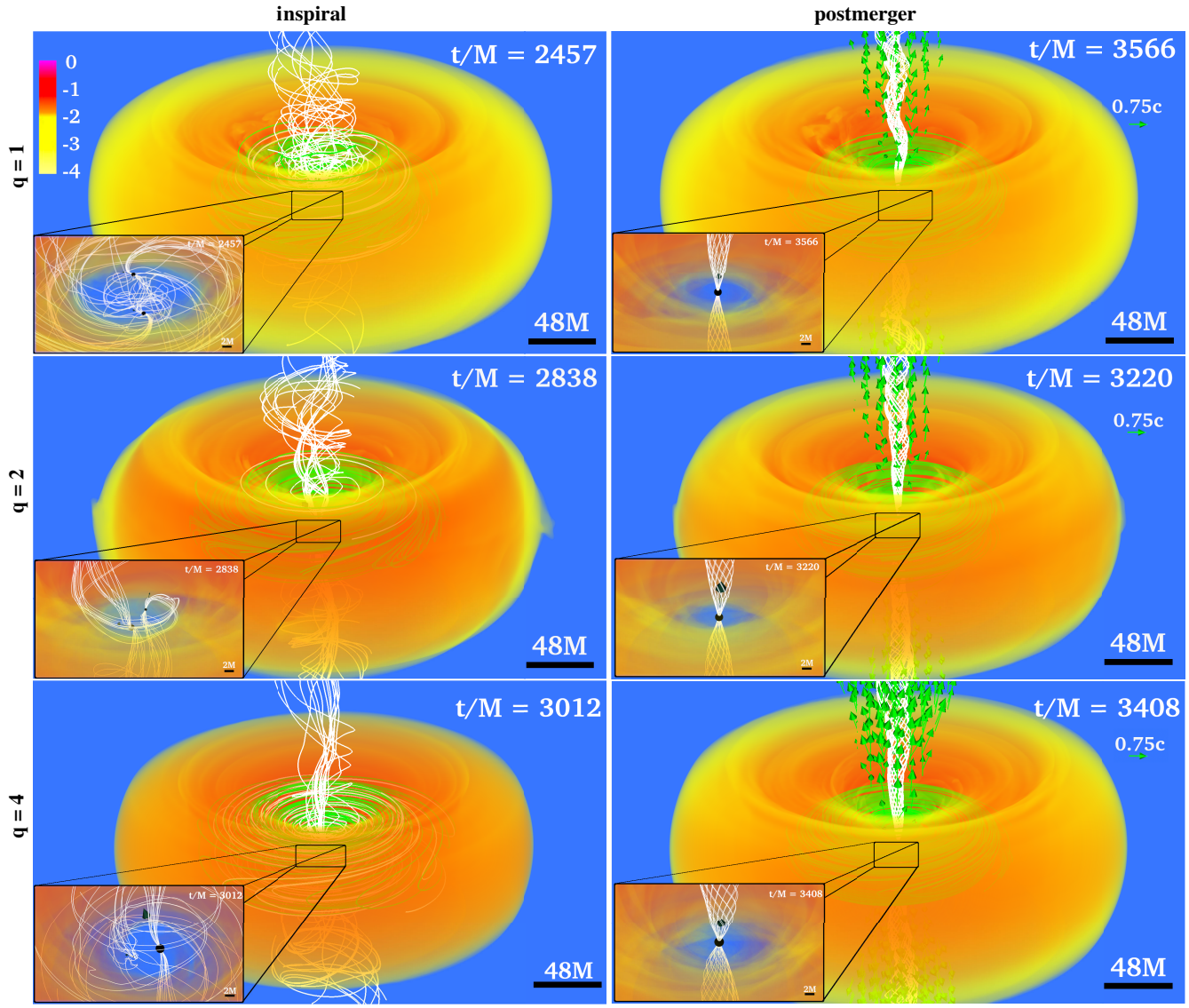

FIG. 6. Volume rendering of the rest-mass density profile, normalized to the initial maximum density, during the predecoupling (left column) and postmerger rebrightening/afterglow phases (right column). Also shown are the magnetic field lines emanating from the poles of the apparent horizon (white) and those in the disk (green) for all cases in Table I. The arrows indicate the fluid velocities while the BH apparent horizons are displayed as black objects. The insets highlight the direction (not the magnitude) of the BH spin and the field lines once an outflow has been launched.

system. See insets on the left column in Fig. 6 for other cases. This effect leads to a dual jet structure in the vicinity of the BHs that resembles the one reported in [9]. Here $r_{\rm BH}$ is the radius of the apparent horizon.

Figure 7 displays the force-free parameter on a meridional slice during the predecoupling epoch (see top and bottom-left panels). In the vicinity of the primary BHs' poles, this parameter reaches values $\sim$100 for cases with mass ratio $q > 1$. However, for the secondary BHs and those with $q = 1$, its values reach at most $b^2/(2\rho_0) \sim 10$ (see inset in Fig. 7). This behavior is anticipated because the pileup of the matter inside the Hill sphere of the latter BH maintains a higher density and lower force-free parameter (see Sec. III A). The larger values of $b^2/(2\rho_0)$ help to tighten the magnetic field in the funnel, leading to a more collimated helical structures. This explains why the primary BH for cases with $q > 1$ has a narrower funnel than that above the poles of the secondary BH (see bottom inset in Fig. 6). As the magnetic-to-gas-pressure increases, persistent outflows confined within the BH funnels are launched and merge into a single one at larger distance $r \gg 10r_{\rm BH}$ (see Fig. 7). As shown on the right column in Fig. 6, incipient jets persist during the whole evolution. Similar results have been observed in [11] once the BHBH-cloud of matter reaches a quasistationary state. As pointed out in [9], these

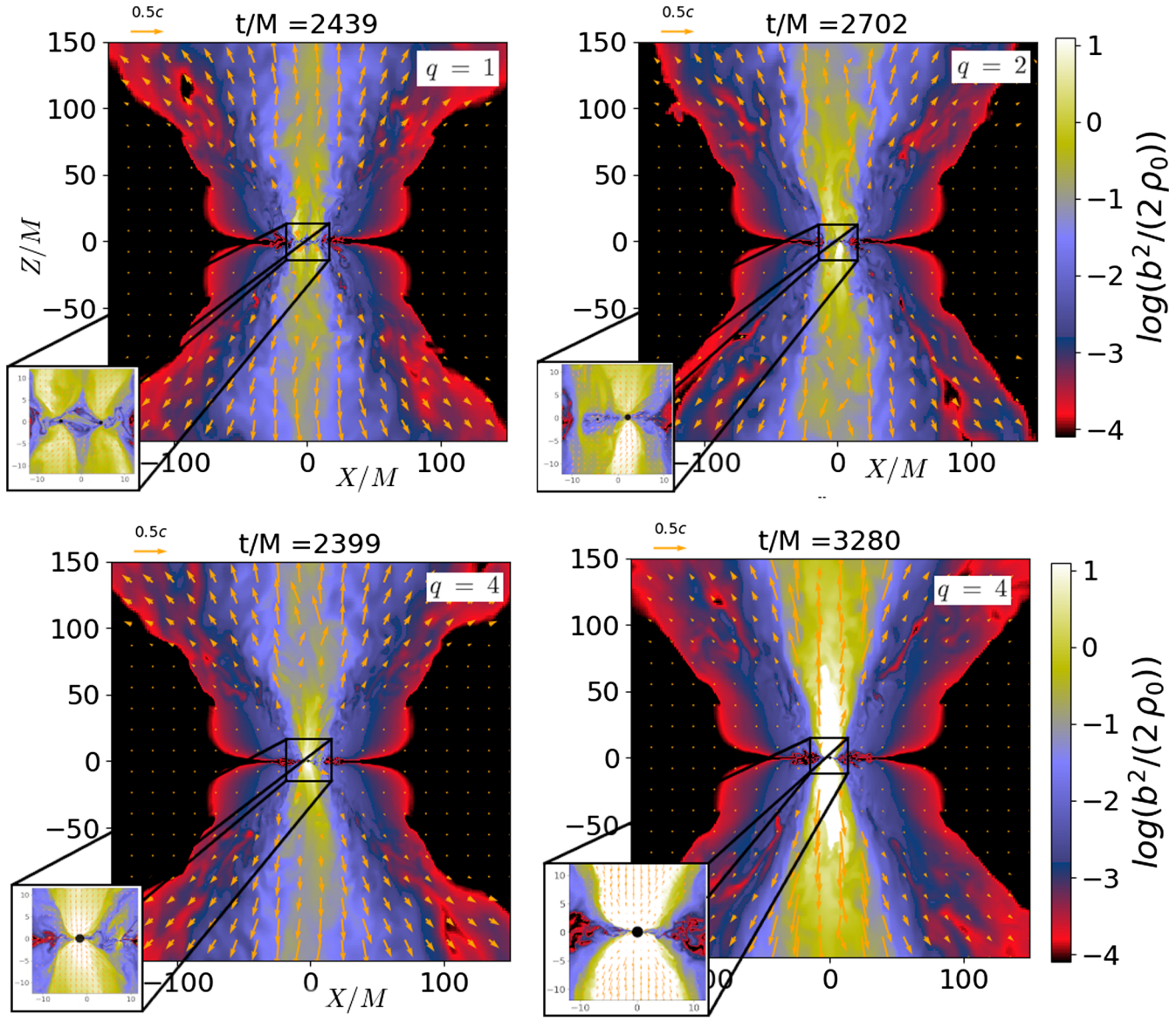

FIG. 7. Force-free parameter $b^2/(2\rho_0)$ (log scale) on a meridional plane during the predecoupling phase for all cases in Table I (top and bottom-left panels) and during the postmeger rebrightening/afterglow phase for $q = 4$ case (bottom-right panel). Similar results are found for the other cases considered here. The arrows indicate the fluid velocities, while the BH apparent horizons are displayed as black objects. The inset highlights the force-free parameter in the vicinity of the BH apparent horizons.

results suggest that it is unlikely that EM signatures from the individual jets can be detectable, contrary to what has been suggested in previous force-free simulations [105]. As we described previously, during the predecoupling phase, the binary carves out a partial hollow where accretion streams constantly feed the BHs. Therefore, a force-free prescription everywhere as considered in [105] may not be suitable to model this system.

During the merger, a significant fraction of the orbital angular momentum of the binary is transferred to that of the remnant BH causing an appreciable increase in the magnitude and a sudden reorientation of its spin with respect to those spins of the progenitors (see Fig. 2). Simultaneously, the two funnels merge into a single tightly wound, collimated, helical magnetic funnel pointing along the direction of the BH spin remnant. As the latter spin increases by a factor $\gtrsim 2$ with respect to those of the progenitor (see Table III), and the inner disk's edge flows inward, the outflow collimates even further. During this period, we observe that magnetically dominated regions with values $b^2/(2\rho_0) \gtrsim 100$ rapidly expand to heights larger than $r \sim 100 r_{\rm BH}$ (see bottom-right panel in Fig. 7). This is a typical effect of the BH spin on the magnetic field lines that has been observed in different astrophysical scenarios involving compact binary mergers (see e.g. [2,3,11,31,32,105]).

After merger, the sudden reorientation of the BH spin, and hence of the magnetic field lines, induces the formation of a kink that propagates along the helical magnetic funnel. We track its propagation using our 3D visualizations of the magnetic field lines every $\Delta t \simeq 0.5M$ and find that, regardless the mass ratio, the kink is damped in $\Delta t \lesssim 15M$ following its formation, leaving no memory of the reorientation of the BH spins. Similar behavior can be inferred from other misaligned studies (see e.g. bottom-right panel in Fig. 2 in [11]). Our results from these exploratory simulations suggest that x-shaped radio galaxies may not be formed through galaxy mergers containing misaligned, low-spin ($\chi \lesssim 0.6$) SMBHs in low-mass disks and hence, rule out the spin shifters as an unique mechanism to explain x-shaped radio galaxies if the accretion onto the BH is stochastic as previously claimed (see e.g. [50,51]). Other events may therefore be necessary to induce helical distortions leading to an x-shaped jet. For example, the interactions between the jet and the shells of stars and debris that form and rotate around the merged galaxy may cause temporary deflections of the jets, creating the observe of structure [106]. Alternatively, precession of a highly spinning BH in self-gravitating, massive disk may provide another explanation [18].

We track the Lorenz factor $W = \alpha_c u^0$ of the flow inside regions where $b^2/(2\rho_0) \geq 10^{-2}$, our definition of the funnel's boundary. Here α_c is the lapse function. During the predecoupling phase, and once the accretion rate has reached a quasisteady state, we observe that the maximum value of the Lorentz factor depends only slightly on the mass ratio. At a modest distance from the BHs ($r \gtrsim 30 r_{\rm BH}$), $W \sim 1.1$ for $q = 1$ while $W \sim 1.2$ and 1.3 for $q = 2$ and $q = 4$, respectively, and hence, the larger the mass ratio, the larger the Lorentz factor of the mildly relativistic outflow. However, this behavior is reversed after merger, where it is found that $W \sim 2.6$ for $q = 1$, $W \sim 2.1$ for $q = 2$ and $W \sim 1.6$ for $q = 4$. This relative change is likely due to the magnitude of the spin of the BH remnant (see Table III). As mentioned before, the lower the binary mass ratio, the larger the spin of the BH remnant, which drives a more confined fluid beam within a more collimated, tightly wound, helical magnetic field. Note that steady-state and axisymmetric jet models show that the maximum attainable value of W at large distance is approximately equal to $b^2/(2\rho_0)$ [107], which reaches values $\gtrsim$100 within the funnel. Therefore, material in the above funnels may be accelerated to $W \sim 100$, as required to explain γ-ray burst phenomenology.

We compute the EM Poynting flux $L_{\rm EM} = -\int T^{\rm r(EM)}_t \sqrt{-g} d\mathcal{S}$ across a spherical surface $\mathcal{S}$ with a coordinate radius $r_{\rm ext}$. To verify that $L_{\rm EM}$ is $r_{\rm ext}$ independent, we vary the extraction radius from $r_{\rm ext} = 120M$ to $r_{\rm ext} = 300M$, finding values in reasonable agreement. Here g is the full spacetime metric determinant, and $T^{\mu({\rm EM})}_\nu$ is the

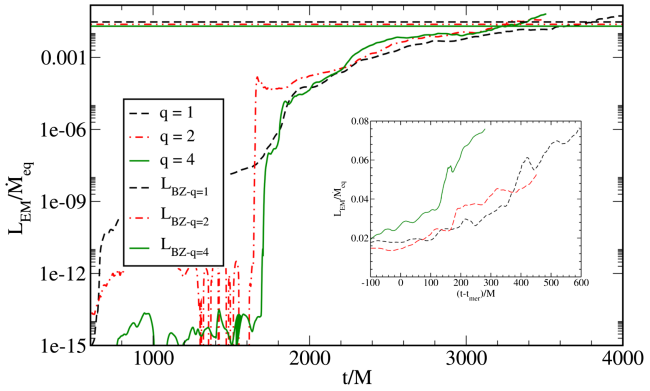

FIG. 8. Poynting luminosity $L_{\rm EM}$ for cases in Table I normalized to the time-averaged accretion rate onto the BH remnant over the last $\Delta t \sim 500M$ before the termination of our simulations (i.e. the radiative efficiency). The horizontal lines indicate the expected Blandford-Znajek luminosity $L_{\rm BZ}$ from a single BH with the same mass, spin and quasistationary polar magnetic field strength as those found for the BH-disk remnant in each simulated case. The inset focuses on the postmerger phase showing a moderate boost in the outgoing Poynting luminosity.

EM stress-energy tensor. Figure 8 displays $L_{\rm EM}$ as a function of time for all cases in Table I. During the predecoupling phase, we observe that the EM luminosity in the $q = 1$ case increases smoothly during the first $\sim$6 quasicircular orbits ($t \sim 1600M$; see bottom panel in Fig. 5) followed by a sudden boost of roughly 3 orders of magnitude in only $\sim$1.6 orbits [$\Delta t \sim 230M \simeq 0.36(M/10^6 M_\odot)(1+z)$ h or $\Delta t \sim 230M \simeq 14(M/10M_\odot)\times(1+z)$ ms]. After this, $L_{\rm EM}$ smoothly ramps up reaching a nearly constant value of $L_{\rm EM} \sim 0.015\dot{M}_{\rm eq}$ as the accretion rate reaches a quasiequilibrium state (see Fig. 5). Here $\dot{M}_{\rm eq}$ is the time-averaged accretion rate onto the BH remnant over the last $\Delta t \sim 500M$ before the termination of our simulation. Presumably the preequilibrium rise is due to the system adjusting to our adopted initial conditions, where a vacuum exists around the binary. Similar behavior is observed in $q = 4$ though the luminosity increases by a factor of $\sim 10^2$ in $\sim$1 orbit [$\Delta t \sim 100M \simeq 0.14(M/10^6 M_\odot)\times(1+z)$ h or $\Delta t \sim 100M \simeq 5(M/10M_\odot)(1+z)$ ms]. After that, it smoothly increases until it reaches the nearly constant value $\sim 0.010\dot{M}_{\rm eq}$. This behavior is not evident in $q = 2$ where the luminosity jumps discontinuously from almost null values to a nearly constant value of $\sim 0.012\dot{M}_{\rm eq}$. Once the BH remnant settles, we compute the efficiency defined as $\epsilon_{\rm EM} \equiv L_{\rm EM}/\dot{M}_{\rm eq}$ and find that the smaller the mass ratio the larger the $\epsilon_{\rm EM}$ (see Table III). This is most likely due to the fact that the poloidal magnetic flux, which has been found to be one of the major determining factors for the efficiency of the outgoing EM (Poynting) luminosity in MHD BH-accretion disk systems (see e.g. [108,109]), is larger when the binary mass ratio is smaller.

Following the merger, the magnitude of the Poynting luminosity in all cases gets a new, but rather moderate, boost (see inset in Fig. 8). A more substantial rise likely occurs in the radiation from the disk, including a thermal component [56]. In contrast to the nonspinning GRMHD BHBH-disk simulations we reported in [31], where it was found that during the postmerger phase the boost in the outgoing Poynting luminosity decreases as the mass ratio increases, we observe that $L_{\rm EM}$ is boosted by roughly a factor of ~ 4 regardless the mass ratio. These results may indicate that the effects of the BH spin on this luminosity have a stronger impact during the predecoupling phase. As in [31], we also observe a time delay between the binary merger and the boost, which depends on the mass ratio. In particular, we find that in $q = 1$, the increase in the luminosity takes place at $\Delta t \sim 425M \simeq 0.6(M/10^6 M_\odot)(1+z)$ h [or $\Delta t \sim 425M \simeq 2.1(M/10M_\odot)(1+z)$ ms] after the merger, while in $q = 4$, it occurs at $\Delta t \sim 160M \simeq 0.2(M/10^6 M_\odot)(1+z)$ h [or $\simeq 0.8(M/10M_\odot)(1+z)$ ms], and hence, the larger the binary mass ratio, the shorter the time delay. A similar effect has been found by fixing the mass ratio but changing the disk thickness in [34].

As the BHs are spinning with nearly force-free fields inside their jet funnels, one may attribute the Poynting luminosity to the Blandford-Znajek mechanism [42], which is typically invoked to describe the emission from the force-free magnetospheres above the poles of single, spinning BHs (see e.g. [110]). Following the merger, we compute the expected Blandford-Znajek EM luminosity $L_{\rm BZ}$ [see Eq. (4.50) in [111]] from a single BH with the same mass and spin parameter χ as the remnants in the postmerger phase of our simulations (see Table III) and the quasistationary polar magnetic field strength time-averaged over the last $\Delta t \sim 500M$ before the termination of our simulations: $L_{\rm BZ} \sim 10^{51}\chi^2(M_{\rm BH}/10^6 M_\odot)^2(B/10^5 G)^2$ erg s^{-1} [or $L_{\rm BZ} \sim 10^{51}\chi^2(M_{\rm BH}/10M_\odot)^2(B/10^{16}G)^2$ erg s^{-1}]. As displayed in Fig. 8, $L_{\rm BZ}$ is roughly consistent with the $L_{\rm EM}$ extracted from our simulations, and hence, we can attribute this luminosity and accompanying magnetically power jet from the spinning BH-disk remnant system to the Blandford-Znajek mechanism. This value is also consistent with the narrow range of values predicted for the jet luminosity for *all* such as systems, independent of mass scale [112].

V. DISCUSSION

The advance of "multimessenger astronomy" promises to resolve a number of long-standing astrophysical puzzles, such as the origin of γ-ray bursts, the nature of matter at supranuclear densities, the formation channels of supermassive black holes, etc. However, to understand these observations and, specifically to understand the interplay between general relativity, GW and EM signals, and the underlying microphysics, it is crucial to compare observations to predictions from theoretical modeling. In particular, multimessenger observations of accreting black holes, single and binaries, call for a detailed understanding of the environment surrounding them and the knowledge of some characteristic GW and EM signatures that can be used to distinguish these systems from other compact objects and determining their parameters.

As a step forward in this goal, we extended our previous GRMHD simulations of binary black holes in magnetized, circumbinary disks [9,29,31,34] by considering misaligned, spinning binary black holes undergoing merger with mass ratios $q = M_{1,\rm irr}/M_{2,\rm irr} = 1, 2$ and 4. The magnitude of the individual, dimensionless, black hole spin is $\chi \equiv S/M_{\rm i,irr}^2 = 0.26$, consistent with a stochastic accretion in AGN (see e.g. [50,51]), lying either along the initial orbital plane or 45° above it.

We evolved these configurations starting from the end of the predecoupling phase all the way to the merger and rebrightening/afterglow phase to identify their Poynting EM emission features and to analyze their dependence on the black hole spin and the binary mass ratio. We also discussed whether the spin shift of the black hole remnant with respect to those of the progenitors leaves an observable imprint in the outgoing Poynting luminosity, surrounding medium profile or in the magnetically driven jet that can be used to characterize the spin properties of merging black hole binaries or give new insight into the formation channels of x-shaped radio galaxies [52,53] and searches for such systems (see e.g. [54]).

During the predecoupling phase, we observed that a magnetically driven (dual) outflow emerges from the poles of the two black holes, pointing along the direction of their spin as long as the force-free parameter within the funnel satisfies $b^2/(2\rho_0) = B^2/(8\pi\rho_0) \gtrsim 1$. At large distance, where the values of this parameter drops to $\lesssim 1$, the twin jets merge, generating a single outflow. These results are consistent with the GRMHD studies of highly spinning BHs in which the spin is tilted with respect to the initial orientation of an uniform magnetic field in [113]. They found that a helical magnetic field emerges from the BH poles along the direction of its spin but only out to a coordinate radius $r \gtrsim 30M$. This effect may prevent the EM detection of the individual jets, as has been suggested previously [55]. During this phase, we also found that the accretion rate exhibits a quasiperiodic behavior with a dominant frequency $2\pi f_{\rm c} \simeq (3/4)\Omega_{\rm BHBH}$ that is mass ratio independent. Here $\Omega_{\rm BHBH}$ is the average orbital frequency of the binary. Simultaneously, we observed that, depending on the mass ratio, the outgoing Poynting luminosity is significantly boosted during $\sim 0.14 - 0.36(M/10^6 M_\odot)(1+z)$ h [or $\sim 5 - 14(M/10M_\odot)(1+z)$ ms] after the start of the simulations, though this may be an artifact of our initial conditions, which are characterized, by a vacuum close to the binary. Consistent with [31], and after quasiequilibrium

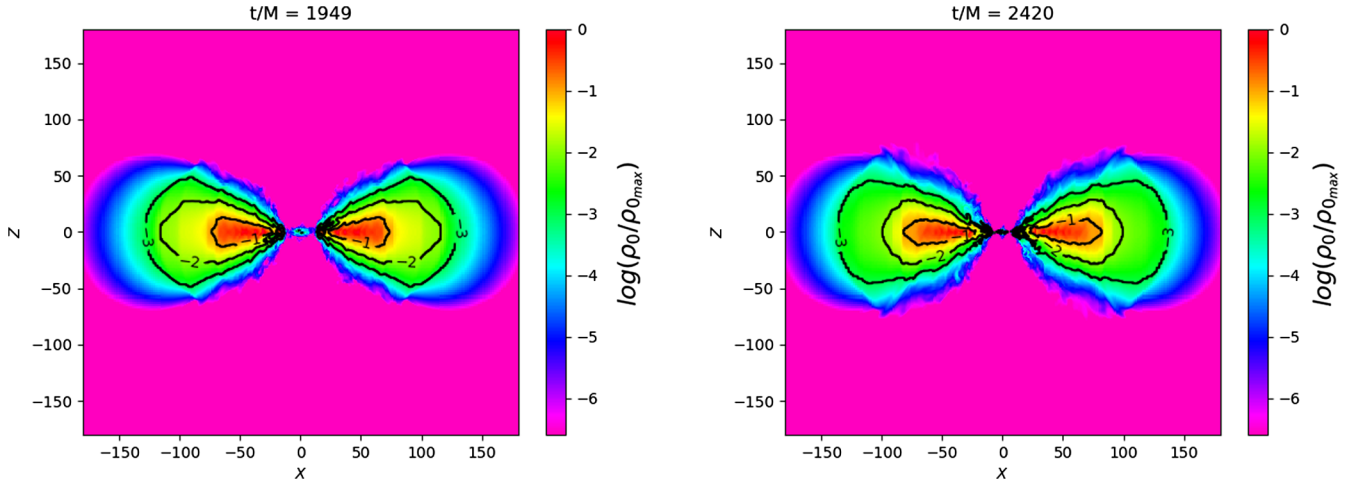

FIG. 9. Rest-mass density ρ_0 on the xz plane at selected times during the predecoupling phase for $q = 1$ case. The density countours (continuous lines) do not change significantly during the late decoupling phase, demonstrating that the disk has relaxed on average. Similar results are found among all cases considered in Table I.

accretion is achieved, we observed a new, but moderate, boost in the luminosity during the rebrightening/afterglow phase following merger that is nearly mass ratio independent. These sudden changes can alter the Poynting emission across the jet and may be used to distinguish black hole binaries in AGNs from single accreting black holes based only on jet morphology in NGC 5128-like sources [31].

During and after the merger, we tracked the field lines emanating from the black hole apparent horizon and observed a kink perturbation propagating along the funnel (see [114]). The kink can be attributed to the spin reorientation of the black hole remnant with respect to the spins of the progenitors. Using our 3D visualizations every $\Delta \sim 0.5M$, we followed this perturbation and found that it is quickly damped in a few M, leaving no memory of the spin reorientation. Similar results were inferred from the misaligned spinning black hole binary immersed in a magnetized cloud of matter [11]. These results may suggest that the spin reorientation mechanism following binary black hole mergers may not be a plausible scenario to explain x-shaped radio galaxies, at least in low-mass disks and low-spin black holes. Note that if stochastic accretion onto supermassive black holes is taking place, which naturally induces low spinning BHs, then additional mechanisms, such as jet interaction with the environment [106], remnant black hole precession, due to tidal torques and/or gravitomagnetic precession in a more massive ambient disks, may be required to explain this scenario. A few caveats remain. First, our results assume that once the accretion rate reaches a quasisteady state ($t \sim 1500M$), the disk has relaxed. Further evidence is indicated by our comparison of density contours (see Fig. 9), which do not move at late times. Although our analysis supports that assumption, a longer inspiral phase from larger separation may be required to ensure the relaxation of the disk and therefore corroborate the present results. Second, we do not consider radiation transfer in our simulations. The inclusion of magnetic effects along with a self-consistent radiation transfer scheme are both needed to accurately determine the flow, the accretion rate onto the BHs, and the EM luminosity and spectra from the strong-field regions near the BHs. We plan to implement such a scheme and address the aforementioned issues in future studies.

Movies and additional 3D visualizations highlighting our simulations can be found at [114] under the same title as this paper.

ACKNOWLEDGMENTS

We thank members of our Illinois Relativity Undergraduate Research Team (M. Kotak, J. Huang, E. Yu, and J. Zhou) for assistance with some of the 3D visualizations. This work was supported in part by National Science Foundation (NSF) Grants No. PHY-2006066 and No. PHY-2308242, and the National Aeronautics and Space Administration (NASA) Grant No. 80NSSC17K0070 to the University of Illinois at Urbana-Champaign. M. R. acknowledges support by the Generalitat Valenciana Grant CIDEGENT/2021/046 and by the Spanish Agencia Estatal de Investigación (Grant No. PID2021-125485NB-C21). A. T. acknowledges support from the National Center for Supercomputing Applications (NCSA) at the University of Illinois at Urbana-Champaign through the NCSA Fellows program. This work made use of the Extreme Science and Engineering Discovery Environment (XSEDE), which is supported by NSF Grant No. TG-MCA99S008. This research is also part of the Frontera computing project at the Texas Advanced Computing Center. Frontera is made

possible by NSF Award No. OAC-1818253. Resources supporting this work were also provided by the NASA High-End Computing Program through the NASA Advanced Supercomputing Division at Ames Research Center. The authors thankfully acknowledge the computer resources at MareNostrum and the technical support provided by the Barcelona Supercomputing Center (AECT-2023-1-0006).

[1] K. Kyutoku, M. Shibata, and K. Taniguchi, Living Rev. Relativity **24**, 5 (2021).
[2] L. Baiotti and L. Rezzolla, Rep. Prog. Phys. **80**, 096901 (2017).
[3] M. Ruiz, S. L. Shapiro, and A. Tsokaros, Front. Astron. Space Sci. **8**, 39 (2021).
[4] D. Richstone *et al.*, Nature (London) **395**, A14 (1998), https://arxiv.org/abs/astro-ph/9810378.
[5] K. Gebhardt *et al.*, Astrophys. J. Lett. **539**, L13 (2000).
[6] A. De Rosa *et al.*, New Astron. Rev. **86**, 101525 (2019).
[7] M. Milosavljevic and E. S. Phinney, Astrophys. J. Lett. **622**, L93 (2005).
[8] P. Artymowicz and S. H. Lubow, Astrophys. J. **421**, 651 (1994).
[9] R. Gold, V. Paschalidis, Z. B. Etienne, S. L. Shapiro, and H. P. Pfeiffer, Phys. Rev. D **89**, 064060 (2014).
[10] M. Ruiz, R. N. Lang, V. Paschalidis, and S. L. Shapiro, Astrophys. J. Lett. **824**, L6 (2016).
[11] F. Cattorini, S. Maggioni, B. Giacomazzo, F. Haardt, M. Colpi, and S. Covino, Astrophys. J. Lett. **930**, L1 (2022).
[12] D. Kocevski, N. Omodei, and G. Vianello (Fermi-LAT Collaboration), arXiv:1710.05450.
[13] K. Akiyama *et al.* (Event Horizon Telescope Collaboration), Astrophys. J. Lett. **875**, L4 (2019).
[14] K. C. Chambers *et al.*, arXiv:1612.05560.
[15] R. Williams, *Hubble Deep Field and the Distant Universe* (IOP Publishing, Bristol, United Kingdom, 2018), pp. 2514–3433.
[16] M. W. McElwain *et al.*, Publ. Astron. Soc. Pac. **135**, 058001 (2023).
[17] E. Wessel, V. Paschalidis, A. Tsokaros, M. Ruiz, and S. L. Shapiro, Phys. Rev. D **103**, 043013 (2021).
[18] A. Tsokaros, M. Ruiz, S. L. Shapiro, and V. Paschalidis, Phys. Rev. D **106**, 104010 (2022).
[19] M. Bailes, Nat. Rev. Phys. **3**, 344 (2021).
[20] R. Abbott *et al.* (LIGO Scientific and Virgo Collaborations), arXiv:2108.01045.
[21] J. P. W. Verbiest, S. Oslowski, and S. Burke-Spolaor, *Handbook of Gravitational Wave Astronomy* (Springer, Singapore, 2021).
[22] P. Amaro-Seoane, H. Audley, and S. Babak, arXiv:1702.00786.
[23] N. I. Shakura and R. A. Sunyaev, Astron. Astrophys. **24**, 337 (1973), https://ui.adsabs.harvard.edu/abs/1973A&A....24..337S.
[24] M. A. Abramowicz, B. Czerny, J. P. Lasota, and E. Szuszkiewicz, Astrophys. J. **332**, 646 (1988).
[25] S. Ichimaru, Astrophys. J. **214**, 840 (1977).
[26] R. Narayan, ASP Conf. Ser. **121**, 75 (1997), https://arxiv.org/abs/astro-ph/9611113.
[27] B. Giacomazzo, J. G. Baker, M. C. Miller, C. S. Reynolds, and J. R. van Meter, Astrophys. J. **752**, L15 (2012).
[28] S. C. Noble, B. C. Mundim, H. Nakano, J. H. Krolik, M. Campanelli, Y. Zlochower, and N. Yunes, Astrophys. J. **755**, 51 (2012).
[29] B. D. Farris, R. Gold, V. Paschalidis, Z. B. Etienne, and S. L. Shapiro, Phys. Rev. Lett. **109**, 221102 (2012).
[30] B. D. Farris, P. Duffell, A. I. MacFadyen, and Z. Haiman, Astrophys. J. **783**, 134 (2014).
[31] R. Gold, V. Paschalidis, M. Ruiz, S. L. Shapiro, Z. B. Etienne, and H. P. Pfeiffer, Phys. Rev. D **90**, 104030 (2014).
[32] B. J. Kelly, J. G. Baker, Z. B. Etienne, B. Giacomazzo, and J. Schnittman, Phys. Rev. D **96**, 123003 (2017).
[33] D. B. Bowen, V. Mewes, M. Campanelli, S. C. Noble, J. H. Krolik, and M. Zilhão, Astrophys. J. Lett. **853**, L17 (2018).
[34] A. Khan, V. Paschalidis, M. Ruiz, and S. L. Shapiro, Phys. Rev. D **97**, 044036 (2018).
[35] K. Akiyama *et al.* (Event Horizon Telescope Collaboration), Astrophys. J. Lett. **875**, L1 (2019).
[36] K. Akiyama *et al.* (Event Horizon Telescope Collaboration), Astrophys. J. Lett. **930**, L12 (2022).
[37] M. Janssen *et al.* (Event Horizon Telescope Collaboration), Nat. Astron. **5**, 1017 (2021).
[38] D. A. Cosandey, Astrophys. Space Sci. **367**, 92 (2022).
[39] N. Neumayer, A. Seth, and T. Böker, Astron. Astrophys. Rev. **28**, 4 (2020).
[40] H. Tagawa, S. S. Kimura, Z. Haiman, R. Perna, and I. Bartos, Astrophys. J. Lett. **946**, L3 (2023).
[41] V. Strokov, G. Fragione, and E. Berti, Mon. Not. R. Astron. Soc. **524**, 2033 (2023).
[42] R. D. Blandford and R. L. Znajek, Mon. Not. R. Astron. Soc. **179**, 433 (1977).
[43] A. Corral, R. Della Ceca, A. Caccianiga, P. Severgnini, H. Brunner, F. J. Carrera, M. J. Page, and A. D. Schwope, Astron. Astrophys. **530**, A42 (2011).
[44] B. P. Abbott *et al.* (LIGO Scientific and Virgo Collaborations), Phys. Rev. Lett. **116**, 241102 (2016).
[45] V. Connaughton *et al.*, Astrophys. J. Lett. **826**, L6 (2016).
[46] V. Paschalidis, J. Bright, M. Ruiz, and R. Gold, Astrophys. J. Lett. **910**, L26 (2021).
[47] J. C. Bright and V. Paschalidis, Mon. Not. R. Astron. Soc. **520**, 392 (2023).

[48] E. M. Gutiérrez, L. Combi, S. C. Noble, M. Campanelli, J. H. Krolik, F. G. L. Armengol, and F. García, Astrophys. J. **928**, 137 (2022).
[49] L. Combi, F. G. L. Armengol, M. Campanelli, B. Ireland, S. C. Noble, H. Nakano, and D. Bowen, Phys. Rev. D **104**, 044041 (2021).
[50] A. R. King, J. E. Pringle, and J. A. Hofmann, Mon. Not. R. Astron. Soc. **385**, 1621 (2008).
[51] S. Nayakshin, C. Power, and A. R. King, Astrophys. J. **753**, 15 (2012).
[52] J. P. Leahy and A. G. Williams, Mon. Not. R. Astron. Soc. **210**, 929 (1984).
[53] Gopal-Krishna, P. L. Biermann, and P. J. Wiita, Astrophys. J. Lett. **594**, L103 (2003).
[54] D. H. Roberts, L. Saripalli, and R. Subrahmanyan, Astrophys. J. Lett. **810**, L6 (2015).
[55] C. Palenzuela, T. Garrett, L. Lehner, and S. L. Liebling, Phys. Rev. D **82**, 044045 (2010).
[56] S. L. Shapiro, Phys. Rev. D **87**, 103009 (2013).
[57] A. R. King, S. H. Lubow, G. I. Ogilvie, and J. E. Pringle, Mon. Not. R. Astron. Soc. **363**, 49 (2005).
[58] J.-M. Wang, C. Hu, Y.-R. Li, Y.-M. Chen, A. R. King, A. Marconi, L. C. Ho, C.-S. Yan, R. Staubert, and S. Zhang, Astrophys. J. Lett. **697**, L141 (2009).
[59] G. Lodato and D. Gerosa, Mon. Not. R. Astron. Soc. **429**, L30 (2013).
[60] K. Iwasawa *et al.*, Mon. Not. R. Astron. Soc. **282**, 1038 (1996).
[61] A. C. Fabian, S. Vaughan, K. Nandra, K. Iwasawa, D. R. Ballantyne, J. C. Lee, A. De Rosa, A. Turner, and A. J. Young, Mon. Not. R. Astron. Soc. **335**, L1 (2002).
[62] L. W. Brenneman and C. S. Reynolds, Astrophys. J. **652**, 1028 (2006).
[63] C. S. Reynolds, Classical Quantum Gravity **30**, 244004 (2013).
[64] C. F. Gammie, S. L. Shapiro, and J. C. McKinney, Astrophys. J. **602**, 312 (2004).
[65] T. Bogdanovic, M. C. Miller, and L. Blecha, Living Rev. Relativity **25**, 3 (2022).
[66] M. Coleman Miller and J. H. Krolik, Astrophys. J. **774**, 43 (2013).
[67] M. Liska, A. Tchekhovskoy, A. Ingram, and M. van der Klis, Mon. Not. R. Astron. Soc. **487**, 550 (2019).
[68] A. I. Macfadyen and M. Milosavljevic, Astrophys. J. **672**, 83 (2008).
[69] B. Kocsis, Z. Haiman, and A. Loeb, Mon. Not. R. Astron. Soc. **427**, 2680 (2012).
[70] D. J. Muñoz and Y. Lithwick, Astrophys. J. **905**, 106 (2020).
[71] R. Miranda and D. Lai, Mon. Not. R. Astron. Soc. **452**, 2396 (2015).
[72] J.-M. Shi, J. H. Krolik, S. H. Lubow, and J. F. Hawley, Astrophys. J. **749**, 118 (2012).
[73] M. Zilhão, S. C. Noble, M. Campanelli, and Y. Zlochower, Phys. Rev. D **91**, 024034 (2015).
[74] F. G. L. Armengol, L. Combi, M. Campanelli, S. C. Noble, J. H. Krolik, D. B. Bowen, M. J. Avara, V. Mewes, and H. Nakano, Astrophys. J. **913**, 16 (2021).
[75] S. C. Noble, J. H. Krolik, M. Campanelli, Y. Zlochower, B. C. Mundim, H. Nakano, and M. Zilhão, Astrophys. J. **922**, 175 (2021).
[76] D. B. Bowen, V. Mewes, S. C. Noble, M. Avara, M. Campanelli, and J. H. Krolik, Astrophys. J. **879**, 76 (2019).
[77] J. E. Pringle, Mon. Not. R. Astron. Soc. **248**, 754 (1991).
[78] B. Kocsis, N. Yunes, and A. Loeb, Phys. Rev. D **84**, 024032 (2011).
[79] J.-M. Shi and J. H. Krolik, Astrophys. J. **807**, 131 (2015).
[80] F.-K. Liu, X.-B. Wu, and S. L. Cao, Mon. Not. R. Astron. Soc. **340**, 411 (2003).
[81] M. Dovciak, F. Muleri, R. W. Goosmann, V. Karas, and G. Matt, Mon. Not. R. Astron. Soc. **391**, 32 (2008).
[82] S. L. Shapiro, Phys. Rev. D **81**, 024019 (2010).
[83] J. D. Schnittman and J. H. Krolik, Astrophys. J. **684**, 835 (2008).
[84] B. D. Farris, P. Duffell, A. I. MacFadyen, and Z. Haiman, Mon. Not. R. Astron. Soc. **447**, L80 (2015).
[85] S. A. Balbus and J. F. Hawley, Rev. Mod. Phys. **70**, 1 (1998).
[86] S. L. Shapiro and S. A. Teukolsky, *Black Holes, White Dwarfs, and Neutron Stars: The Physics of Compact Objects* (Wiley-Interscience, New York, 1983), p. 663.
[87] P. C. Peters, Phys. Rev. **136**, 1224 (1964).
[88] M. Ansorg, B. Bruegmann, and W. Tichy, Phys. Rev. D **70**, 064011 (2004).
[89] M. Campanelli, C. O. Lousto, Y. Zlochower, B. Krishnan, and D. Merritt, Phys. Rev. D **75**, 064030 (2007).
[90] B. D. Farris, Y. T. Liu, and S. L. Shapiro, Phys. Rev. D **84**, 024024 (2011).
[91] J.-P. De Villiers, J. F. Hawley, and J. H. Krolik, Astrophys. J. **599**, 1238 (2003).
[92] B. D. Farris, Y. T. Liu, and S. L. Shapiro, Phys. Rev. D **81**, 084008 (2010).
[93] M. D. Duez, Y. T. Liu, S. L. Shapiro, and M. Shibata, Phys. Rev. D **73**, 104015 (2006).
[94] Z. B. Etienne, Y. T. Liu, and S. L. Shapiro, Phys. Rev. D **82**, 084031 (2010).
[95] CactusConfigs, http://www.cactuscode.org.
[96] E. Schnetter, S. H. Hawley, and I. Hawke, Classical Quantum Gravity **21**, 1465 (2004).
[97] Carpet, Carpet Code homepage.
[98] M. Shibata and T. Nakamura, Phys. Rev. D **52**, 5428 (1995).
[99] T. W. Baumgarte and S. L. Shapiro, Phys. Rev. D **59**, 024007 (1999).
[100] Z. B. Etienne, J. A. Faber, Y. T. Liu, S. L. Shapiro, K. Taniguchi, and T. W. Baumgarte, Phys. Rev. D **77**, 084002 (2008).
[101] I. Hinder *et al.*, Classical Quantum Gravity **31**, 025012 (2014).
[102] Z. B. Etienne, V. Paschalidis, Y. T. Liu, and S. L. Shapiro, Phys. Rev. D **85**, 024013 (2012).
[103] D. J. D'Orazio, Z. Haiman, and A. MacFadyen, Mon. Not. R. Astron. Soc. **436**, 2997 (2013).

[104] T. Bogdanovic, C. S. Reynolds, and M. C. Miller, Astrophys. J. Lett. **661**, L147 (2007).
[105] C. Palenzuela, L. Lehner, and S. L. Liebling, Science **329**, 927 (2010).
[106] Gopal-Krishna, P. L. Biermann, L. A. Gergely, and P. J. Wiita, Res. Astron. Astrophys. **12**, 127 (2012).
[107] N. Vlahakis and A. Konigl, Astrophys. J. **596**, 1080 (2003).
[108] K. Beckwith, J. F. Hawley, and J. H. Krolik, Astrophys. J. **678**, 1180 (2008).
[109] J. C. McKinney, A. Tchekhovskoy, and R. D. Blandford, Mon. Not. R. Astron. Soc. **423**, 3083 (2012).
[110] J. C. McKinney and C. F. Gammie, Astrophys. J. **611**, 977 (2004).
[111] K. S. Thorne, R. H. Price, and D. A. MacDonald, *Black Holes: The Membrane Paradigm* (Yale University Press, New Haven, Connecticut, 1986).
[112] S. L. Shapiro, Phys. Rev. D **95**, 101303 (2017).
[113] B. J. Kelly, Z. B. Etienne, J. Golomb, J. D. Schnittman, J. G. Baker, S. C. Noble, and G. Ryan, Phys. Rev. D **103**, 063039 (2021).
[114] 3D visualizations highlighting our results can be found at: https://research.physics.illinois.edu/CTA/movies.